Supporting Information

Tvrdy et al. 10.1073/pnas.1011972107

SI Text

Derivation of Eq. 4. In our model, the quantum dot (QD) is modeled as a sphere with radius R_{QD} and dielectric permittivity ε_{QD}. The radial dependence of the delocalized hole wavefunction in the QD is written as

$$\Psi(r) = \frac{\sin(\frac{\pi r}{R_{QD}})}{r\sqrt{2\pi R_{QD}}}. \quad [S1]$$

Corresponding charge density inside the QD is

$$\rho(r) = -e|\Psi(r)|^2 = -e\frac{\sin^2(\frac{\pi r}{R_{QD}})}{2\pi R_{QD} r^2} \quad [S2]$$

and $\rho = 0$ outside. According to the Gauss theorem, the radial component of the electric field is

$$D(r) = \frac{1}{r^2}\int_o^r \rho(x)x^2 dx. \quad [S3]$$

For $r > R_{QD}$, Eq. **S3** gives the coulomb formula

$$D(r) = -\frac{e}{r^2}. \quad [S4]$$

Inside the QD($r < R_{QD}$), the field is

$$D(r) = -\frac{e}{rR_{QD}}\left(1 - \frac{\sin(\frac{2\pi r}{R_{QD}})}{2\pi r}R_{QD}\right). \quad [S5]$$

The charging energy is given by the following expression:

$$E_c = \int_0^\infty \frac{[D(r)]^2}{2\varepsilon_{QD}(r)} r^2 dr, \quad [S6]$$

where $\varepsilon_{QD}(r)$ is radius-dependent dielectric permittivity. The parameter $\varepsilon_{QD}(r)$ is equal to one outside the dot and ε_{QD} inside. Substitution of Eqs. **S4** and **S5** into Eq. **S6** gives

$$E_c = \int_0^{R_{QD}} \frac{e^2}{2\varepsilon_{QD} r^2 {R_{QD}}^2}\left(1 - \frac{\sin(\frac{2\pi r}{R_{QD}})}{2\pi r}R_{QD}\right)^2 r^2 dr + \int_{R_{QD}}^\infty \frac{e^2}{2r^4} r^2 dr. \quad [S7]$$

After numerical integration,

$$E_c = \frac{e^2}{2R_{QD}} + \frac{e^2}{2\varepsilon_{QD}R_{QD}}\left(1 - \frac{\mathrm{Si}(2\pi)}{\pi} + \frac{\mathrm{Si}(4\pi)}{2\pi}\right) = \frac{e^2}{2R_{QD}} + \frac{e^2}{2\varepsilon_{QD}R_{QD}}C \quad [S8]$$

where $\mathrm{Si}(x)$ is the integral sine function, $C \approx 0.786$. The charging energy cannot be expressed analytically if the QD is placed close to the dielectric wall (oxide particle) having dielectric permittivity ε_{MO} (MO, metal oxide). The income of the QD–wall interaction can be estimated under the assumption that all the charge is homogeneously distributed on the surface. In this case, the interaction term is the following:

$$\Delta E_c = -\frac{e^2}{4(R_{QD}+h)}\frac{\varepsilon_{MO}-1}{\varepsilon_{MO}+1} \quad [S9]$$

where h is the QD-wall distance. Finally, combining Eq. **S8**, which increases system energy due to charging of the particle, with Eq. **S9**, which decreases system energy due to interaction of that charge with the neighboring dielectric, yields

$$E_c \approx \frac{e^2}{2R_{QD}}\left(1 + \frac{C}{\varepsilon_{QD}}\right) - \frac{e^2}{4(R_{QD}+h)}\frac{\varepsilon_{MO}-1}{\varepsilon_{MO}+1}. \quad [S10]$$

Note that Eq. **S10** accounts for the energetic costs of moving an electron from the quantum dot to the metal oxide particle, which leaves behind a single charged hole in the quantum dot.

From these formulations, we can compute the overall change in system free energy by considering the entire system in its initial state (before the electron transfer):

$$E_i \approx E_{1Se} + E_{1S_{3/2}} - (1+C)\frac{e^2}{\varepsilon_{QD}R_{QD}} \quad [S11]$$

where E_{1Se} and $E_{1S_{3/2}}$ are the electron and hole energy, respectively. The last term is the coulomb interaction between delocalized electron and hole in the QD (1). The energy of the system after the electron transfer to the oxide particle

$$E_f = E_{MO} + E_{1S_{3/2}} + E_c, \quad [S12]$$

where E_{MO} is the energy of the electron at the MO conduction band edge. Thus, the total free energy gap of the reaction is

$$\Delta G = E_f - E_i \approx E_{MO} - E_{1Se} + (1+C)\frac{e^2}{\varepsilon_{QD}R_{QD}} + \frac{e^2}{2R_{QD}}\left(1 + \frac{C}{\varepsilon_{QD}}\right) - \frac{e^2}{4(R_{QD}+h)}\frac{\varepsilon_{MO}-1}{\varepsilon_{MO}+1}, \quad [S13]$$

where Eq. **4** is a simplified form of Eq. **S13**. Using the values listed in Table S1, along with a separation distance of $h = 0$, we were able to calculate the ΔG values listed in Table 1.

Further Discussion of Uncertainty in Effective Mass for Metal Oxides Used in This Study. It is important to first note that, in terms of our analysis of Eq. **1**, there exists two scaling terms which have yet to be determined with a great degree of experimental or theoretical certainty. The first, $\tilde{H}(E)$, which we assume to be independent of energy, but not necessarily independent of MO species, represents the overlap between the donating and accepting state wavefunctions. Models for this term have been used previously to describe coupling between all organic donor–acceptor pairs (2), however, no such model exists for acceptors composed of a continuum of states with varying density. Despite a lack of a theoretical model, this term was utilized previously to account for discrepancies between theoretical and experimental data in electron transfer rates from Re-bipyridyl complexes to TiO_2 and SnO_2 nanoparticles, reporting $\tilde{H}(E)$ values of 100 and 350 cm^{-1} for the two metal oxides, respectively (3).

The second scaling factor arises from the portion of $\rho(E)$ which includes the bulk density of states. This term includes the effective mass of the accepting metal oxide species, m_e^*, which is independent of energy, and thus contributes to Eq. **1** as a scaling

factor. In terms of the three metal oxide particles under investigation—SnO_2, TiO_2, and ZnO—experimental reports of effective mass range in value from $(0.30–0.35)m_0$ (4, 5), $(0.71 \geq 10)m_0$ (4, 6–8), and $(0.22–0.30)m_0$ (1, 8, 9), respectively, where m_0 is the electron rest mass. Given the relative uncertainty in both of these scaling factors, this study limited its discussion of agreement between experimental data and Eq. **1** to, first, an assignment of reorganizational energy λ, which can be estimated well as the energy corresponding to the sharp rise in the k_{ET} vs. ΔG plot (Fig. 3), and, second, estimations for values of $\tilde{H}(E)$, the accuracy of which is limited to the accuracy of previously reported values of the other scaling factor, $m_e{}^*$. Estimated values of $\tilde{H}(E)$ and $m_e{}^*$ are codependent, such that an overestimation of $m_e{}^*$ results in an underestimation of $\tilde{H}(E)$ and vice versa.

Detailed Experimental Materials, Methods, and Measurements. ***Materials.*** Acetonitrile (Fisher, HPLC grade); tri-*n*-octylphosphine oxide (TOPO, Acros, 99%); *n*-tetradecylphosphonic acid (TDPA, PCI Synthesis); 1-dodecylamine (DDA, Alfa, 98 + %); selenium powder (Se, Aldrich, 100 mesh, 99.5%); cadmium oxide (CdO, Alfa, 99.998%); trioctylphosphine (TOP, Aldrich, 90%); toluene (Fisher, HPLC grade); methanol (Fisher, laboratory grade); SiO_2 nanoparticles (Nalco 2327; diameter, 20 nm); tin oxide nanoparticles (SnO_2 NP solution, Alfa, 15% in H_2O colloidal dispersion; diameter, 15 nm); zinc oxide nanoparticles (ZnO NP solution, Alfa, NanoArc® 40% in H_2O colloidal dispersion; diameter, 30 nm); titaniaum dioxide paste (TiO_2 Paste, Dyesol, DSL 90-T; diameter, 20 nm); polyethylene glycol (PEG, Alfa, average molecular weight of 12,000); copper sulfate ($CuSO_4$, Matheson Coleman and Bell, 99 + %); sodium sulfide (Na_2S, Sigma), Sulfur (S, Baker); sodium hydroxide (NaOH, Fisher), nickel wire [Ni Wire, Alfa; diameter, 0.5 nm, annealed, 99.5% (metals basis)]; and water (deionized, filtered) were used.

Synthesis and Purification of CdSe Quantum Dots. CdSe quantum dots were synthesized as previously described (10). In brief, CdO, TDPA, and DDA were dissolved in TOPO at 110 °C. The system was degassed, purged with nitrogen, and subsequently heated to approximately 300 °C. A mixture of TOP and 1 M TOPSe was injected and CdSe nanoparticle size grew with increased temperature. Following synthesis, the reaction flask was cooled and nitrogen-purged toluene was added. This solution was centrifuged (10 min., $20{,}000 \times g$) to separate excess DDA and other unreacted materials. QDs were then flocculated from solution using nitrogen-purged methanol and redispensed in nitrogen-purged toluene. This process was repeated three times to remove excess TOPO from the mixture and QD surface. QDs were stored in fresh, nitrogen-purged toluene inside of a nitrogen glove box.

Construction of Nanoparticulate Metal Oxide Thin Films. Semitransparent nanopaticulate metal oxide thin films were made by either doctor blading or spin-coating mixtures of native metal oxide nanoparticles. SiO_2 NP films were made by spin coating ~100 μL of 400 mg PEG per milliliter of 1:1 Nalco 2327 SiO_2:H_2O (by volume). SnO_2 NP films were made by doctor blading 700 mg PEG per milliliter of SnO_2 NP solution. TiO_2 NP films were made by doctor blading the as received Dyesol TiO_2 paste. ZnO NP films were made by spin coating ~100 μL of 100 mg PEG per milliliter ZnO NP solution. All spin-coats were done at $150 \times g$ for 12 s. Films were spin-coated or doctor bladed onto either glass microscope slides (~0.5× 1.5 cm for spectroscopic measurements) or fluorine doped tin oxide transparent electrodes (~0.8 × 2 cm for photoelectrochemical measurements). All films were annealed for 1 h at 450 °C to burn off residuals and sinter the NP network. Following annealing, film thicknesses, as measured by Alpha Step 500 surface profilometer, were determined to be 4, 6, 6, and 5 μm, for SiO_2, SnO_2, TiO_2, and ZnO, respectively. Crystallinity of MO films were confirmed by X-ray diffraction (XRD) and determined to be 100% cassiterite, anatase, and wurtzite SnO_2, TiO_2, and ZnO, respectively (see Fig. S4 for XRD patterns).

Sensitization of Nanoparticulate Metal Oxide Thin Films with CdSe QDs. Preannealed nanoparticulate metal oxide thin films were heated to ~200 °C inside a glove box and immersed directly into a >1 μM (number of QDs per liter) solution of QDs in toluene. The QDs adsorbed directly onto the metal oxide substrates over the course of 48 h. The films were then removed from the CdSe solution, rinsed with nitrogen-purged toluene, and allowed to dry. Films intended for optical measurements were placed inside of a sealed optical cell for evacuation before removal from the glove box, whereas those intended for photoelectrochemical measurements were removed from the glove box and characterized. A visual description of the procedure utilized to sensitize MO films, along with images of both optical and photoelectrochemical cells, is shown in Fig. 2.

Optical Measurements. Transmission absorption spectra were recorded using a Cary Bio 50 spectrophotometer. Diffuse reflectance absorption spectra were recorded using a Shimadzu UV-3101PC spectrophotometer. Emission spectra were recorded using a Jobin Yvon Horiba Florolog spectrofluorometer. Transient absorption measurements were conducted using a Clark-MXR 2010 (775 nm, 1 mJ/pulse, FWHM = 130 fs, 1 kHz repetition) laser system coupled with detection software from Ultrafast Systems (Helios). The pump–probe (pump 95% of fundamental, frequency doubled to 387 nm; probe 5% of fundamental used to generate white light continuum) beams were incident on the sample (room temperature) at an angle <10°. The probe beam was collected with a CCD spectrograph (Ocean Optics, S2000-UV-Vis) providing a 430–750-nm data window. Typically, 1,500 excitation pulses were averaged to obtain a transient spectrum at a set delay time. All optical measurements on films were conducted in an evacuated 2-mm path length quartz cell to prevent film degradation (10).

Photoelectrochemical Measurements. Photoelectrochemical measurements were made using a Princeton Applied Research potentiostat PARSTAT 2263 and a two electrode cell using a nickel supported Cu_2S counterelectrode and Na_2S (0.1 M) solution as the redox couple. The (Ni)Cu_2S counterelectrode was assembled by immersing a Ni wire in a Cu_2SO_4 aqueous solution along with a zinc source (such as a US penny cut into fourths). Forming an electrical connection between the two yielded a copper coating on the nickel wire. The wire was then removed and immersed in a 1 M Na_2S, 1 M S, 1 M NaOH solution for 12 h to convert the thin copper coating to copper sulfide. Experiments were conducted using a spectrum generated by passing light from a 150 W xenon lamp through an air mass 1.5 filter, and normalizing a 0.28 cm^2 spot to 100 mW/cm^2. Incident photon-to-carrier generation efficiency measurements were made by coupling the aforementioned light source with a Bausch and Lomb high-intensity monochromator (FWHM ~ 15 nm). Cell currents were measured using a Keithley 617 electrometer and normalized to wavelength-dependent incident power using a silicon photodiode.

1. Brus LE (1984) Electron-electron and electron-hole interactions in small semiconductor crystallites: The size dependence of the lowest excited electronic state. *J Chem Phys* 80:4403–4409.

2. Kemnitz K, Nakashima N, Yoshihara K (1988) Electron-transfer by isolated rhodamine-B molecules adsorbed on organic single-crystals—a solvent-free model system. *J Phys Chem* 92:3915–3925.

3. She CX, et al. (2005) pH-dependent electron transfer from re-bipyridyl complexes to metal oxide nanocrystalline thin films. *J Phys Chem B* 109:19345–19355.
4. Ai X, Guo JC, Anderson NA, Lian TQ (2004) Ultrafast electron transfer from Ru polypyridyl complexes to Nb_2O_5 nanoporous thin films. *J Phys Chem B* 108:12795–12803.
5. Nagasawa M, Shionoya S, Makishim S (1965) Electron effective mass of SnO_2. *J Phys Soc Japan* 20:1093–1093.
6. Stamate MD (2003) On the non-linear I-V characteristics of dc magnetron sputtered TiO_2 thin films. *Appl Surf Sci* 205:353–357.
7. Tang H, Prasad K, Sanjines R, Schmid PE, Levy F (1994) Electrical and optical-properties of TiO_2 anataste thin-films. *J Appl Phys* 75:2042–2047.
8. Enright B, Fitzmaurice D (1996) Spectroscopic determination of electron and hole effective masses in a nanocrystalline semiconductor film. *J Phys Chem* 100:1027–1035.
9. Haase M, Weller H, Henglein A (1988) Photochemistry and radiation chemistry of colloidal semiconductors. *J Phys Chem* 92:482–487.
10. Tvrdy K, Kamat PV (2009) Substrate driven photochemistry of CdSe quantum dot films: Charge injection and irreversible transformation on oxide surfaces. *J Phys Chem A* 113:3765–3772.

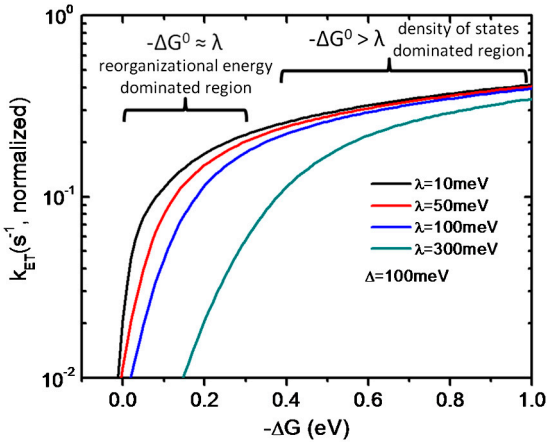

Fig. S1. The dependence of k_{ET} vs. ΔG for various reorganizational energies, λ, in a metal oxide nanocrystal with Gaussian-shaped band edge defects of width $\Delta = 100$ meV.

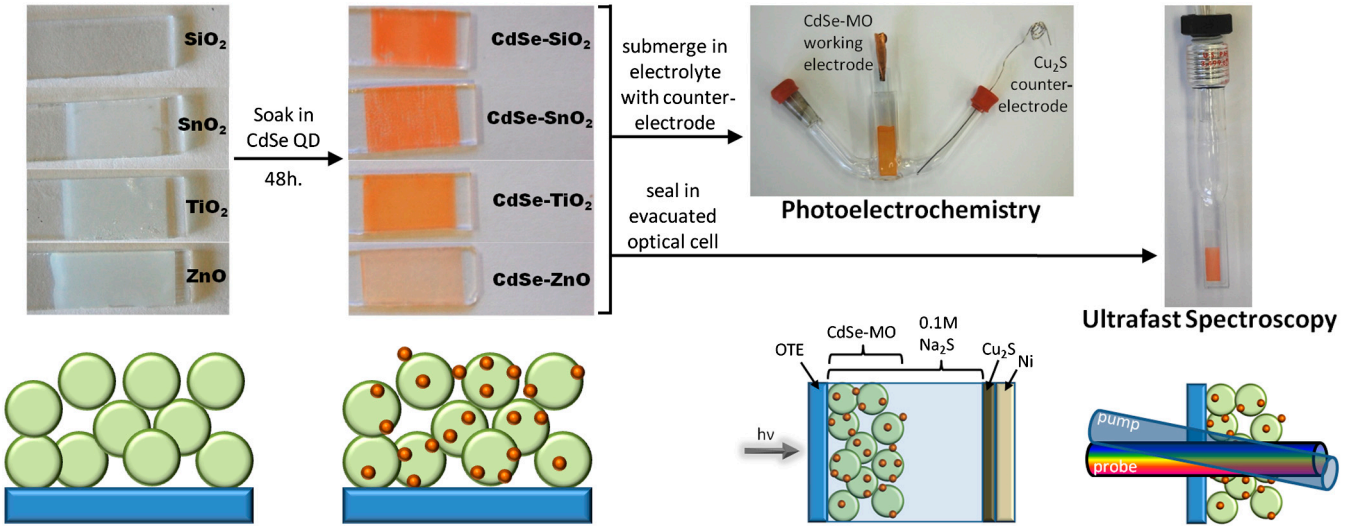

Fig. S2. Images of the four nanoparticulate metal oxide thin films utilized in this study (SiO_2, SnO_2, TiO_2, and ZnO) before and after sensitization with CdSe quantum dots. Also shown are cells designed to allow measurement of both photoelectrochemical and ultrafast spectroscopic (under vacuum) properties of the sensitized films.

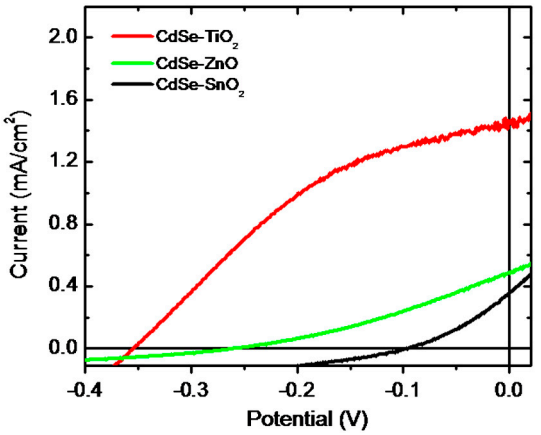

Fig. S3. I–V characteristics of films presented in *Application—Photovoltaic Measurements* section of the main text.

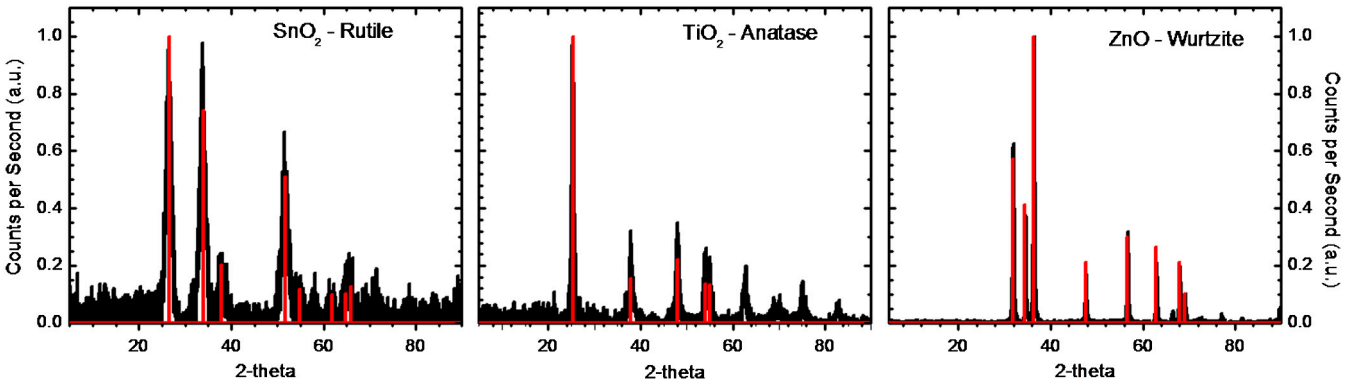

Fig. S4. Powder X-ray diffraction patterns of the three electron accepting metal oxide species used in this study. Red-line stick diagrams represent position and relative amplitudes of peaks associated with rutile SnO_2 (1), anatase TiO_2 (2), and wurtzite ZnO (3).

1 Haines J, Leger JM (1997) X-ray diffraction study of the phase transitions and structural evolution of tin dioxide at high pressure: Relationships between structure types and implications for other rutile-type dioxides. *Phys Rev B* 55:11144–11154.
2 Djerdj I, Tonejc AM (2006) Structural investigations of nanocrystalline TiO_2 samples. *J Alloys Compd* 413:159–174.
3 Yoshio K, Onodera A, Satoh H, Sakagami N, Yamashita H (2001) Crystal structure of ZnO:Li at 293 K and 19 K by X-ray diffraction. *Ferroelectrics* 264:133–138.

Table S1. List of values used to calculate ΔG for the quantum dot-metal oxide systems utilized in this study

	R, nm	ε	Ref(s).	E_{OX}, eV	E_{1Se}, eV
CdSe	1.4	6.1	1		−3.65
CdSe	1.65	6.1	1		−3.78
CdSe	2.0	6.1	1		−3.89
CdSe	2.1	6.1	1		−3.94
SnO_2		11.5	2	−4.88	
TiO_2		9.9	3	−4.41	
ZnO		10.5	4	−4.36	

1. Djerdj I, Tonejc AM (2006) Structural investigations of nanocrystalline TiO_2 samples. *J Alloys Compd* 413:159–174.
2. She CX, et al. (2005) pH-dependent electron transfer from re-bipyridyl complexes to metal oxide nanocrystalline thin films. *J Phys Chem B* 109:19345–19355.
3. Ai X, Guo JC, Anderson NA, Lian TQ (2004) Ultrafast electron transfer from Ru polypyridyl complexes to Nb_2O_5 nanoporous thin films. *J Phys Chem B* 108:12795–12803.
4. Nagasawa M, Shionoya S, Makishim S (1965) Electron effective mass of SnO_2. *J Phys Soc Japan* 20:1093–1093.

Table S2. Numerical summary of common photoelectrochemical parameters for the three films depicted in Fig. 6 *A* and *B*

Working electrode	I_{sc}, mA/cm^2	V_{oc}, V	FF	η, %
CdSe-SnO_2	0.36	0.094	0.20	0.066
CdSe-TiO_2	1.46	0.35	0.39	0.20
CdSe-ZnO	0.49	0.26	0.19	0.024

I_{sc}, short circuit current; V_{oc}, open circuit voltage; FF, fill factor ; η, power conversion efficiency.